Renewable Energy 152 (2020) 198–207

Contents lists available at ScienceDirect

Renewable Energy

journal homepage: www.elsevier.com/locate/renene

Robust optimal aiming strategies in central receiver systems

Sascha Kuhnke [a, *], Pascal Richter [b], Fynn Kepp [a], Jeff Cumpston [c], Arie M.C.A. Koster [a], Christina Büsing [a]

[a] Lehrstuhl II für Mathematik, RWTH Aachen University, Pontdriesch 10-12, 52062, Aachen, Germany
[b] Steinbuch Centre for Computing, Karlsruhe Institute of Technology (KIT), Hermann-von-Helmholtz-Platz 1, 76344, Eggenstein-Leopoldshafen, Germany
[c] Process Systems Engineering, RWTH Aachen University, Forckenbeckstraße 51, 52074, Aachen, Germany

ARTICLE INFO

Article history:
Received 26 August 2019
Received in revised form
6 November 2019
Accepted 23 November 2019
Available online 28 November 2019

Keywords:
Solar thermal power
Aiming strategy
Robust optimization
Mixed-integer linear programming
Uncertainty quantification

ABSTRACT

A central receiver system is a power plant that consists of a receiver mounted atop of a central tower and a field of adjustable mirrors called heliostats. The heliostats concentrate solar radiation onto the receiver where a fluid is heated to produce electricity in a conventional thermodynamic cycle.

Aiming strategies are used to assign each heliostat to an individual aim point on the receiver such that a given flux distribution on the receiver surface is reached. As uncertainties in the tracking of the heliostats exist, aiming strategies are applied that use large safety margins to avoid dangerously high flux concentrations on the receiver. This approach leads to an inefficient use of the power plant and thus economical losses. In this paper, we consider advanced methods to include these uncertainties into the design of efficient aiming strategies. To this end, we present a mixed-integer linear programming (MILP) formulation for the optimization of aiming strategies based on Γ-robustness.

In a case study, we show that the Γ-robust optimization approach yields solutions with strong objective values and thus economical benefits while maintaining a high degree of safety. Compared to non-robust solutions, the Γ-robust solutions achieve better objective values while guaranteeing the same safety.

1. Introduction

In central receiver systems, large movable mirrors, called heliostats, are used to concentrate rays of sunlight onto a receiver which is mounted on top of a tower. At the receiver, a fluid is heated up. This fluid, typically air, thermal oil or molten salt, transports the heat to a heat exchanger. At the heat exchanger, steam is produced which powers a turbine to generate electricity (see Fig. 1).

Concentration ratios of over 2000 suns are possible at the solar receiver. With this high amount of thermal power being intercepted by the receiver, care must be taken that the receiver does not get damaged in the course of operation. A trade-off between maximizing the receiver intercept and minimizing the peak flux on the receiver must be made. In practice, the operator of the power plant pre-computes a desired flux distribution (DFD) across the receiver surface. For a fixed position of the sun, the task of the aiming strategy is to reach this distribution by directing the heliostats to aim points on the receiver surface while capturing as much radiation as possible. Here, large safety margins are applied to avoid severe damage of the receiver due to high fluxes caused by tracking errors. A tracking error is an uncertainty that may cause the image of a heliostat at the receiver to be offset from the targeted aim point. Reasons for these offsets are the limited accuracy of the motor in the heliostats and inaccuracies in the whole tracking mechanism. While the safety margins ensure a safe operation, an inefficient use of the entire power plant is accepted.

In this work, we show that a robust aiming strategy which directly considers the uncertainty of the tracking error is able to improve the efficiency while maintaining a high degree of safety. This aiming strategy is found by solving a robust optimization problem formulated as a mixed-integer linear program (MILP).

1.1. State of the art

In order to place the current work in context, we present a short description of prior work in which aiming strategies were developed. Previous research on aiming strategies includes the use of specialized heuristics [2–6], the search for optimized aiming

* Corresponding author.
E-mail address: kuhnke@math2.rwth-aachen.de (S. Kuhnke).

https://doi.org/10.1016/j.renene.2019.11.118
0960-1481/

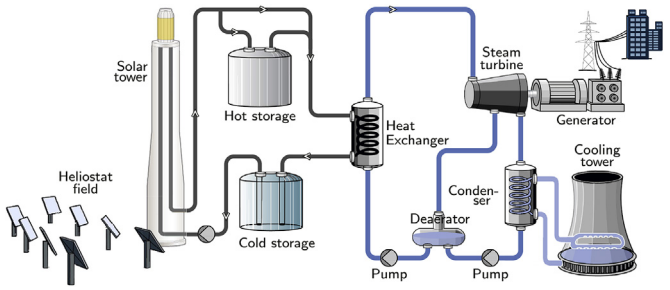

Fig. 1. Conceptual drawing of a central receiver system: Large mirrors in the heliostat field concentrate the sun light onto a receiver which is mounted on top of a tower [1].

Table 1
Summary of previous aim point studies. This work utilizes a robust optimization formulation for the first time in the reviewed literature.

	Receiver Type	Method	Robustness
[2]	Cylindrical/flat plate	6 heuristics	No
[3]	Flat plate	Operating heuristic	No
[4]	Cylindrical	Heuristic	No
[5]	Cylindrical	6 heuristics	No
[6]	Cylindrical	Heuristic	No
[7]	Flat plate	Ant-colony heuristic	No
[8]	Flat plate	Genetic algorithm	No
[9]	Flat plate	MILP formulation	No
This work	**arbitrary**	MILP formulation	**Yes**

strategies using metaheuristics [7,8], and the optimization of aiming strategies by solving an MILP formulation [9]. A summary of previous aim point studies is given in Table 1.

Aim point optimization studies go at least as far back as the work included in the DELSOL optics simulation software [2]. There, a set of fixed aiming strategies is proposed in which the aim points of the heliostats are distributed in specific patterns. Six different path dependent heuristics for solving the problem are contained in the DELSOL 2 software release. Here, heuristics for iteratively placing the flux distributions from each heliostat are available for user selection. These include a smart heuristic that fills the receiver surface with the flux profiles until they impinge on the edge of the receiver. The aiming strategies also allow the user to prioritize either the cold end or the hot end of the receiver.[1]

The complexity of the aim point problem for large heliostat fields is often overcome with the use of simple operating heuristics. For example, García-Martín et al. [3] developed a closed-loop control system using thermo-couples for the circular flat-plate receiver of the PSA CESA-1 plant. The control system balances temperatures by moving heliostats from one aim point of high temperature to one of lower temperature. This is performed iteratively until temperature uniformity is achieved.

A basic heuristic is used for the Gemasolar power plant by Kelly et al. [4] where five possible vertical aim points are allowed and a predefined flux distribution is sought as an objective. This flux distribution is constant in the inner region (about three quarter of the area), and then drops towards the receiver border. The flux distribution in the vertical direction is only considered when choosing aim points for each of the heliostats.

In contrast, Astolfi et al. [5] separate the solar field into azimuthal segments and the flux distribution from each segment is optimized. Despite there being freedom to define the aim point in only the vertical direction, this work accounts for the influence of the lateral distribution on the ideal vertical aim point distribution in adjacent segments. The best method presented in this paper purports to reduce peak flux up to 15%. Collado et al. [6] extended this single-parameter aiming approach (the vertical position) to a two-parameter aiming strategy to flatten the flux profile.

Belhomme et al. [7] propose a solution based on the ant colony optimization meta-heuristic. This method is able to find solutions in up to 15 minutes. Different types of receiver constraints such as maximum heat fluxes or maximum heat flux gradients are considered.

The study by Besarati et al. [8] uses a genetic algorithm with the objective of minimizing the standard deviation of the flux distribution values at each measurement point on the surface. They considered the PSA CESA-1 heliostat field, modified by selecting a subset of heliostats such that the peak flux remains within safety limits when all heliostats are pointed at the center of the receiver.

Ashley et al. [9] formulate the aim point optimization as an MILP and apply this formulation to the PS10 heliostat field. The objective in this case is to maximize the incident energy on the receiver while reaching a uniform flux distribution. Optimal flux distributions are found for a range of different operating conditions. The effect of cloud cover is also simulated.

1.2. Our contribution

In this work, we extend the approach from [9] to first develop a non-robust MILP formulation for the optimization of aiming strategies. This formulation additionally allows to approximate a given DFD to further benefit the energy production. Then, we extend the non-robust formulation to get a robust MILP formulation for the optimization of aiming strategies based on Γ-robustness [10]. In this robust formulation, uncertainties caused by tracking errors are incorporated. The design parameter Γ represents the degree of risk aversion against tracking errors by the operator of the power plant.

In a case study applied to the PS10 solar tower power plant, we show that the resulting robust aiming strategies are superior to the non-robust aiming strategies. The robust solutions increase both the efficiency and safety of the plant. To reduce the running times of the robust approach, we present a heuristic to compute robust aiming strategies in practical running times of less than 60 seconds. Moreover, we conduct a simulation of uncertain tracking errors to show the practicability of the robust solutions. Our approach is applicable to arbitrary receiver types.

We published a preliminary approach for the optimization of aiming strategies in [11]. Here, we extend this preliminary approach by an improved model where the approximation of a given DFD is possible, by an extensive case study as well as by an evaluation of the results via simulations of tracking errors.

1.3. Outline

First, we describe in Section 2 the underlying problem by defining the operational variables and design parameters of a central receiver system that influence the optical performance. In Section 3, an MILP formulation for the non-robust optimization of aiming strategies is given. This formulation is extended in Section 4 to a Γ-robust MILP formulation which considers uncertainties caused by tracking errors. In Section 5, we apply the aiming strategies to the solar tower power plant PS10 in Spain. The solutions of the non-robust and the robust model are compared and the influence of the robustness parameter Γ on the intercepted solar irradiation is investigated. Furthermore, we present a heuristic which yields robust solutions in significantly shorter running times. Finally, we draw in Section 6 a conclusion regarding the presented

[1] This represents an interesting trade-off between high receiver surface temperatures when they are pointed at the hot end and higher overall thermal losses when they are pointed at the cold end.

aiming strategies and give an outlook with possibilities to extend this work.

2. Problem description

This section describes the functionality of a central receiver system along with the optical components which are needed to understand the purpose and effects of aiming strategies.

2.1. Optical components

A central receiver system consists of a *receiver* which is mounted on top of a tower and a large field of *heliostats*. We denote the set of heliostats by H. The heliostats collect the direct normal irradiation of the *sun* on the Earth's surface, denoted by I_{DNI}, and reflect it to the receiver. To adapt for the changing position of the sun, the heliostats are driven by a motor to concentrate the solar irradiation onto the receiver. In our model, the position of the sun is given in terms of the solar zenith and azimuth angle [12]. For the receiver, there exist three different designs:

- *Flat plate receivers* have a rectangular front shape.
- *Cavity receivers* are curved towards the inside of the tower to minimize heat losses as they are sheltered from wind.
- *External receivers* have a cylindrical shape and are attached at the outside of the tower.

The receiver consists of a discrete number of panels in a row and the fluid flows along small tubes which are inside these panels. The flow direction is alternating upwards and downwards along the panels. Due to the high power concentration, the material of the receiver has to withstand high temperatures, temperature gradients in time, and must efficiently transfer the concentrated heat to the flowing medium.

2.2. Aim and measurement points at the receiver

The task of an aiming strategy is to decide for each heliostat at which spot on the receiver surface it should aim. To reduce the difficulty of this task, the aim points on the receiver surface are typically discretized. This means that the heliostats are only allowed to aim at a predefined discrete set of points on the receiver. Here, we use a regular grid as proposed by Ashley et al. [9]. The receiver surface is discretized by the set A containing all possible aim points, i.e.,

$$A = \left\{ a_{i,j} \;\middle|\; i = 1, \dots, n_a^{\text{horiz}}, \quad j = 1, \dots, n_a^{\text{vert}} \right\}$$

where n_a^{horiz} and n_a^{vert} are the number of horizontal and vertical aim points. To evaluate an aiming strategy, we measure the heat flux at certain points on the receiver surface. These measurement points M are arranged in a regular grid similar to the grid of the aim points. It is given by

$$M = \left\{ m_{i,j} \;\middle|\; i = 1, \dots, n_m^{\text{horiz}}, \quad j = 1, \dots, n_m^{\text{vert}} \right\}$$

where n_m^{horiz} and n_m^{vert} are the number of horizontal and vertical measurement points. The left hand side of Fig. 2 shows a visualization of these discretizations.

The set of aim points A is not necessarily the same as the set of measurement points M. In practice, the choice of the number of aim points depends on the relevant flux size of the heliostats. These discretizations can be applied to any receiver shape.

2.3. Desired flux distribution

Before the optimization of the aiming strategy is conducted, a desired flux distribution (DFD) on the receiver surface is defined which is later used as target of the optimization process. In general, these DFD maps are defined by the operator of the central receiver system. They base on CFD simulations conducted by the receiver manufacturer that depend on the receiver material properties and on the possible incident heat flux [13]. The desired flux q_{DFD}^m at the receiver surface is defined point-wise for each measurement point $m \in M$. The right hand side of Fig. 2 illustrates a heat flux distribution on the receiver surface which could be used as a DFD map.

2.4. Heliostat flux distribution

The flux distribution on the receiver surface due to reflection from a particular heliostat targeting a given aim point can be calculated. Starting in the 1970s, several different methods were developed ranging from straight-forward ray tracing methods to mathematical simulation techniques such as cone optics [14], Hermite polynomial expansion, or convolution methods [1]. Altogether, there exist several ray-tracing methods which compute the reflected flux distribution of a heliostat surface onto the receiver surface. The projection on the receiver surface depends on the mirror area, the curvature of the heliostat, the ray's angle of incidence with the heliostat surface (also called cosine efficiency), and on the mirror reflectivity [15].

We now consider a fixed position of the sun. If heliostat $h \in H$ aims at aim point $a \in A$, the reflected flux on the receiver surface at measurement point $m \in M$ is given by q_{ha}^m. Since we have a discrete set of aim points, it is possible to pre-compute all possible flux distributions on the receiver for each heliostat $h \in H$ and each aim point $a \in A$. Hence, we determine one image per heliostat for every aim point beforehand to save time when performing the optimization. The required memory space for the images depends on the number of heliostats, the number of aim points and the number of measurement points.

We use the HFLCAL method [14] to calculate the reflected heat fluxes q_{ha}^m at measurement point $m \in M$ on the receiver surface for each heliostat $h \in H$ aiming at $a \in A$:

$$q_{ha}^m = \frac{P_{ha}}{2\,\pi\,\tilde{\sigma}_{ha}^{\text{effective}}} \cdot \exp\left(-\frac{(x_a^m)^2 + (y_a^m)^2}{2\,\tilde{\sigma}_{ha}^{\text{effective}}} \right) \cdot A^m$$

where

- P_{ha} is the beam power, i.e., the amount of heat reflected from the heliostat which depends on the heliostat, the targeted aim point, and the position of the sun.
- $\tilde{\sigma}_{ha}^{\text{effective}}$ is the effective error that defines the distribution size.
- x_a^m and y_a^m are the distances from measurement point m to aim point a in horizontal and vertical direction, respectively.
- A^m is the receiver area around measurement point m.

To represent a tracking error, we shift the aim point coordinates on the receiver surface which yields different distances x_a^m and y_a^m to the respective measurement points.

For a certain allocation of heliostats to aim points, we can now determine the corresponding heat flux distribution on the receiver surface by linearly superposing the reflected fluxes of each heliostat.

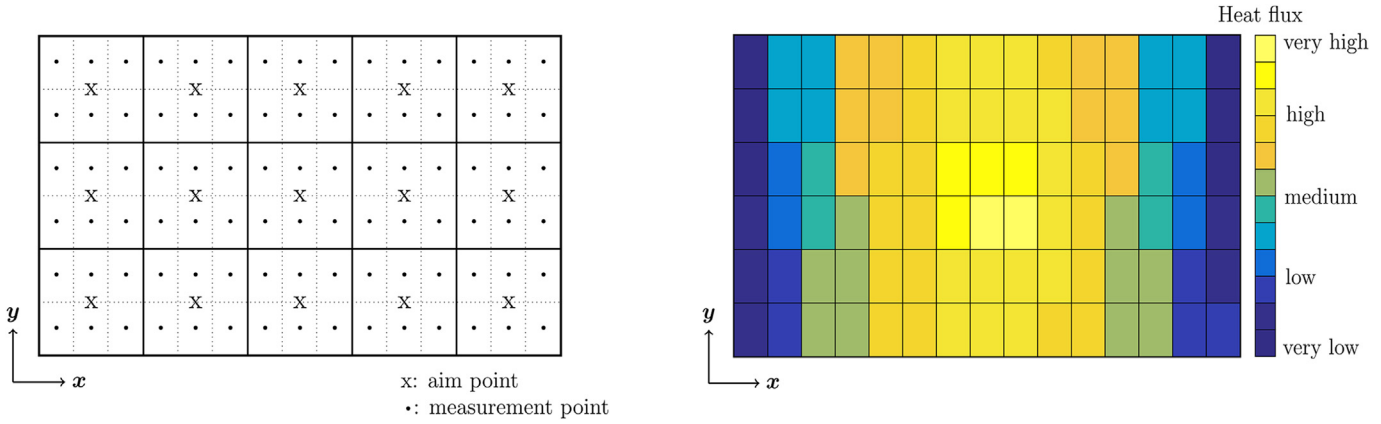

Fig. 2. Discretization of aim and measurement points (left) and heat flux distribution on the receiver surface (right).

2.5. Allowable flux distribution

Due to the nonlinear relationship between radiative thermal losses and heat flux distribution, the relationship between heat flux and receiver surface temperature is modeled prior to optimization. When the maximum allowable receiver surface temperature is known, a corresponding maximum allowable flux is calculated and then imposed as linear constraint during the optimization for the best aiming strategy. The maximum heat flux gradient can also be determined prior to optimization in order to save simulation time. This allows us to formulate the optimization problem using linear constraints, avoiding the increased complexity required to solve problems with nonlinear constraints.

The allowable flux distribution (AFD) defines the maximum solar flux allowable at any given point on the receiver surface during operation. It is dependent on the current operating conditions of the receiver. For a receiver that is operating in thermal equilibrium, there will be an allowable heat flux distribution that corresponds to the differential temperature along the flow direction in the receiver pipes. The AFD is the maximum solar flux that is allowable under the given operating conditions such that the temperature of the receiver surface remains within the material limits. Its values are given by q^m_{AFD} for each measurement point $m \in M$.

The AFD is *time dependent*, and a rapidly increasing flux corresponds to a lower AFD than a slowly increasing flux. This is because the receiver pipe wall must heat up before the increased flux is conveyed to the fluid in the pipes. Thus, for a conservative AFD, calculations of the surface temperature resulting from an increase in solar flux shall be performed assuming any extra heat transfer to the fluid in the receiver be zero.

In the next section, we present a linear formulation of the optimization problem for finding an optimal aiming strategy based on the here presented model.

3. Non-robust aim point optimization model

We now present a mixed-integer linear program (MILP) for the optimization of aiming strategies in central receiver systems. The purpose is to maximize the energy production of the whole power plant while preventing damage to receiver components. In this formulation, we do not consider any uncertainty of the tracking error. This model is based on the formulation of Ashley et al. [9] with the addition that a given desired flux distribution (DFD) is approximated to benefit the energy production.

First, we introduce the decision variables used in the optimization formulation. For each heliostat $h \in H$ and aim point $a \in A$, we introduce binary variables x_{ha} which determine if h aims at a. This means x_{ha} is equal to one if h aims at a and zero otherwise.

Now, we consider the constraints of the optimization model. The first set of constraints ensures that each heliostat aims at most at one aim point, i.e.,

$$\sum_{a \in A} x_{ha} \leq 1 \qquad \forall\ h \in H. \tag{1}$$

Here, the left hand side may be zero which represents the situation that a heliostat aims past the receiver in order to avoid damage due to high heat fluxes. The next constraints ensure that the allowable flux distribution (AFD) is satisfied at each measurement point:

$$\sum_{h \in H} \sum_{a \in A} q^m_{ha}\, x_{ha} \leq q^m_{\text{AFD}} \qquad \forall\ m \in M. \tag{2}$$

In these constraints, the parameters q^m_{ha} are the heat fluxes at measurement point m caused by heliostat h when it aims at aim point a. The parameters q^m_{AFD} are the maximum allowable heat fluxes that must not be exceeded at each m. For the next set of constraints, we consider the desired flux distribution (DFD) which is given by absolute values q^m_{DFD} at each measurement point m. These DFD values depend on the total heat flux currently reaching the receiver. For simplification, we assume that each q^m_{DFD} is equal to a linear expression $q^m_{\text{DFD}} = q^m_{\text{rel}} \cdot \delta$ where $q^m_{\text{rel}} \in [0, 1]$ is a given relative DFD value proportional to q^m_{DFD} and δ is a non-negative continuous variable. The variable δ physically depends on the solar irradiation I_{DNI} and the solar position. Its purpose is to scale the relative values q^m_{rel}. Since the absolute DFD values $q^m_{\text{rel}} \cdot \delta$ can typically not be met exactly, we allow a relative deviation of $\varepsilon > 0$ in both directions from the DFD at each m:

$$(1-\varepsilon)\, q^m_{\text{rel}}\, \delta \leq \sum_{h \in H} \sum_{a \in A} q^m_{ha}\, x_{ha} \leq (1+\varepsilon)\, q^m_{\text{rel}}\, \delta \qquad \forall\ m \in M. \tag{3}$$

While accepting a relative deviation of ε, these constraints ensure that the resulting heat flux distribution on the receiver surface is close to the DFD.

The objective is to maximize the total heat fluxes at all measurement points $m \in M$ on the receiver caused by the current aiming strategy. Therefore, we optimize the following objective function:

$$\max \sum_{m\in M}\sum_{h\in H}\sum_{a\in A} q^m_{ha}\, x_{ha}. \tag{4}$$

The MILP presented here for the optimization of aiming strategies has $|H|\cdot|A|+1$ variables and $|H|+3\,|M|$ constraints. However, as the simulation in Section 5.2 suggests, solutions to this optimization model are very vulnerable against uncertainties caused by tracking errors. Even small deviations of a heliostat from its targeted aim point caused by tracking errors could violate AFD Constraints (2). This poses a high risk of permanent receiver damage. Therefore, we extend this non-robust model by integrating these uncertainties and computing a robust aiming strategy.

4. Robust aim point optimization model

Now, we extend the non-robust optimization model to a robust optimization model where we consider uncertainties of tracking errors. A tracking error causes the image of a heliostat at the receiver to be offset from the targeted aim point. These offsets can result in higher heat fluxes than expected which may cause permanent damage to receiver components even though AFD Constraints (2) are satisfied. Therefore, we consider uncertain data and ensure in our model that Constraints (2) are satisfied for all measurement points m with a high probability:

$$\Pr\Big(\sum_{h\in H}\sum_{a\in A} q^m_{ha}\, x_{ha} \le q^m_{\mathrm{AFD}}\Big) \ge \eta \tag{5}$$

where q^m_{ha} are now random variables and $\eta\in[0,1]$ is the degree of certainty that Constraints (2) are actually fulfilled. However, directly solving this stochastic optimization problem is very difficult [16]. Instead, we use a robust optimization approach to get good feasible solutions for this problem.

Following the approach of Γ-robustness by Bertsimas and Sim [10], we reformulate AFD Constraints (2) by considering default heat fluxes $\overline{q}^m_{ha}$ and their possible deviations $\widehat{q}^m_{ha}$ caused by tracking errors. Since Constraints (2) are upper bounds for the heat fluxes at each measurement point m, it is sufficient to only consider the worst case deviations towards m and ensure that even in case of such a deviation they remain feasible.

To this end, let $\tilde{q}^m_{ha}$ be the heat flux at m if heliostat h targets aim point a but deviates maximally towards m. Assuming h aims at a, this is the worst case heat flux caused by h at measurement point m. Now, we define $\widehat{q}^m_{ha}$ as the worst case deviation from the default heat flux at m, i.e., $\widehat{q}^m_{ha} := \tilde{q}^m_{ha} - \overline{q}^m_{ha}$. It follows for each uncertain heat flux q^m_{ha} that it is part of the interval $q^m_{ha}\in[\overline{q}^m_{ha}, \overline{q}^m_{ha} + \widehat{q}^m_{ha}]$. However, using a robust approach with worst cases will lead to overconservative solutions since it is highly unlikely that all heliostats assume their worst case deviations at the same time. Therefore, we introduce a parameter $\Gamma\in\{0,1,\dots,|H|\}$ which represents the maximum number of heliostats that can deviate simultaneously. For each constraint in (2), we want to ensure feasibility if at most Γ heliostats deviate at the same time. In other words, we want to be protected against deviations caused by all possible subsets of heliostats with at most Γ elements. Therefore, we reformulate AFD Constraints (2) as follows:

$$\sum_{h\in H}\sum_{a\in A}\overline{q}^m_{ha}\, x_{ha} + \mathrm{dev}^m(x) \le q^m_{\mathrm{AFD}} \qquad \forall\ m\in M \tag{6}$$

where

$$\begin{aligned}\mathrm{dev}^m(x) = \max & \sum_{h\in H}\sum_{a\in A}\widehat{q}^m_{ha}\, x_{ha}\, y^m_h\\ \text{s.t.} & \sum_{h\in H} y^m_h \le \Gamma\\ & y^m_h\in\{0,1\} \qquad \forall\ h\in H.\end{aligned}$$

The value $\mathrm{dev}^m(x)$ is the optimal objective value of another optimization problem. It represents the maximum additional heat flux at measurement point m caused by at most Γ deviations from a given allocation of heliostats to aim points x. Here, the binary variables y^m_h denote whether heliostat h deviates towards m or not.

These reformulated constraints are not linear anymore due to the nested optimization problems $\mathrm{dev}^m(x)$. Therefore, we now derive a linear reformulation for Constraints (6) following the approach by Bertsimas and Sim [10]. Since the constraint matrix of the inner optimization problem with optimal objective value $\mathrm{dev}^m(x)$ is totally unimodular (consecutive-ones property is satisfied), the corresponding polyhedron is integral. Consequently, relaxing the integrality of the variables y^m_h does not change the optimal objective value. This allows us to dualize the inner optimization problem and thus we obtain

$$\begin{aligned}\mathrm{dev}^m(x) = \quad \min\ & \Gamma\, z^m + \sum_{h\in H} p^m_h\\ \text{s.t. } & z^m + p^m_h \ge \sum_{a\in A}\widehat{q}^m_{ha}\, x_{ha} \quad \forall\ h\in H\\ & z^m \ge 0\\ & p^m_h \ge 0 \qquad \forall\ h\in H.\end{aligned}$$

Here, the variables z^m for $m\in M$ and p^m_h for $h\in H$ and $m\in M$ of the dual problem are continuous. As Constraints (6) are upper bounds and we are now minimizing the inner optimization problem, it is equivalent to omit the minimization in the objective. This yields the following linear AFD constraints

$$\sum_{h\in H}\sum_{a\in A}\overline{q}^m_{ha}\, x_{ha} + \Gamma\, z^m + \sum_{h\in H} p^m_h \le q^m_{\mathrm{AFD}} \qquad \forall\ m\in M \tag{7}$$

which eventually replace Constraints (2) in the robust optimization problem. Furthermore, the constraints of the dual optimization problems for each measurement point m have to be added to ensure correct evaluation of $\mathrm{dev}^m(x)$. Thus, the Γ-robust optimization formulation is given as follows:

$$\begin{aligned}\max & \sum_{m\in M}\sum_{h\in H}\sum_{a\in A}\overline{q}^m_{ha}\, x_{ha}\\ \text{s.t. } & \sum_{a\in A} x_{ha} \le 1 && \forall\ h\in H\\ & \sum_{h\in H}\sum_{a\in A}\overline{q}^m_{ha}\, x_{ha} + \Gamma\, z^m + \sum_{h\in H} p^m_h \le q^m_{\mathrm{AFD}} && \forall\ m\in M\\ & z^m + p^m_h \ge \sum_{a\in A}\widehat{q}^m_{ha}\, x_{ha} && \forall\ h\in H, m\in M\\ & (1-\varepsilon)\, q^m_{\mathrm{rel}}\, \delta \le \sum_{h\in H}\sum_{a\in A}\overline{q}^m_{ha}\, x_{ha} \le (1+\varepsilon)\, q^m_{\mathrm{rel}}\, \delta && \forall\ m\in M\\ & x_{ha}\in\{0,1\} && \forall\ h\in H, a\in A\\ & \delta \ge 0\\ & z^m \ge 0 && \forall\ m\in M\\ & p^m_h \ge 0 && \forall\ h\in H, m\in M.\end{aligned}$$

Since the derived AFD Constraints (7) are now linear, the presented Γ-robust formulation is an MILP with $(|H|+1)|M|$ additional

variables and $|H|\cdot|M|$ additional constraints.

5. Case study

In this section, we present a case study which applies the two formulations for the optimization of aiming strategies introduced in Section 3 and 4 to the test field PS10. The results of the non-robust model are compared to the results of the Γ-robust model where different degrees of robustness according to the parameter Γ are considered. Furthermore, a simulation of tracking errors motivates the use of the robust optimization model by showing the vulnerability of solutions of the non-robust model.

First, we state in Section 5.1 the setup of the experiments including the central receiver system used in this study, the selected parameters, and specifications about the implementation. In Section 5.2, solutions of the non-robust model are investigated according to simulated tracking errors. In Section 5.3, we present computational results of the non-robust and robust optimization problem along with detail analysis of the calculated solutions. Finally, a discussion of the results can be found in Section 5.4.

5.1. Setup

In this case study, we use real data of the PS10 solar tower power plant which is located near Seville, Spain. With a field of 624 heliostats, this plant is being operated commercially from 2007 [17]. Based on the real positions of the heliostats and the receiver [18], we precalculate all expected heat fluxes $\bar{q}_{ha}^{m}$ and worst case deviations $\hat{q}_{ha}^{m}$ via ray tracing as described in Section 2.4. We assume that the tracking errors are normally distributed with mean $\mu = 0$ and standard deviation $\sigma = 1$ milliradian (see [19], Section 6.3). For the worst case deviations in the Γ-robust models, we assume a maximum horizontal and vertical tracking error of 1.5 milliradian. In the experiments, we apply a grid of 4 horizontal and 5 vertical aim points along with the same grid of measurement points, i.e., $n_a^{\text{horiz}} = n_m^{\text{horiz}} = 4$ and $n_a^{\text{vert}} = n_m^{\text{vert}} = 5$. The original maximum allowable heat flux for the PS10 is at least 650 kW/m^2 (see [18], Section 3). However, since the number of heliostats in this plant is relatively small, no robust approach would be necessary because the original limit 650 kW/m^2 is almost never reached. Therefore, we scale down this original value and use a maximum allowable heat flux $q_{\text{AFD}}^{m} = 200\ kW/m^2$ at each measurement point m. Thus, as in larger power plants with more heliostats, a robust approach is necessary to avoid exceeding the AFD. Lastly, we use a maximum deviation $\varepsilon = 10\,\%$ from a uniform DFD.

For the optimization, we use Java OpenJDK Runtime Environment 11.0.4 along with CPLEX 12.8.0.0 [20] with standard options as MILP solver. All numerical results presented here are computed on a Linux machine with an Intel Core i7-3770 CPU with 3.40 GHz clock rate and 32 GB RAM. Calculations are stopped as soon as an optimality gap of 0.5% or the maximum time limit of 10800 seconds is reached. While each non-robust problem terminated within the desired 0.5% gap with a running time of less than 7 seconds, the robust problems terminated after 3 hours of running time with an average gap of 5.86%. Hence, according to the running time, the non-robust model outperforms the robust model by magnitudes. Therefore, we introduce in Section 5.3 a simple heuristic that strongly reduces the running times of the robust problem. It yields good solutions to the robust problem in running times of around 60 seconds.

5.2. The need of robustness in the optimization model

First, we evaluate whether a robust approach is necessary to protect the receiver from overheating due to tracking errors. To this end, we test the obtained solutions from the non-robust model introduced in Section 3 against simulated tracking errors.

We denote the non-robust optimization problem introduced in Section 3 by DET. A simple approach to add robustness to this problem is to add buffer values to the AFD Constraints (2). By adding a buffer of λ% with $\lambda \in \{0.5, 1, 1.5, \ldots, 17\}$ to the right hand sides of these constraints, we obtain a simple robust problem denoted by DET-λ. For each solution of these problems, we perform a simulation by generating 1000 scenarios. Each of these scenarios simulates the deviations caused by tracking errors according to their normal distribution with mean $\mu = 0$ and standard deviation $\sigma = 1$ milliradian. This means that each scenario yields a different actual heat flux distribution on the receiver surface where some of the AFD Constraints (2) could be violated even though they are not violated in the original solution. We say that a scenario is safe if none of the AFD Constraints is violated in its resulting heat flux distribution. For each solution, we denote the number of safe scenarios among the 1000 scenarios by $|S|$. The relative safety of a solution is equal to $|S|/1000$.

The results of the simulation show that the solution to DET has a safety of 0%, i.e., it is violated in all 1000 scenarios and therefore highly unsafe. Adding buffers improves the safety significantly. The solution to DET-5 achieves already a safety of 66%. However, the risk of severely damaging the receiver is still high. The first solution that achieves a safety of 100% is DET-11. Here, a high degree of safety for the receiver is guaranteed.

These results show that the solution to DET-11 is much more practical than the one to DET since it poses a much lower risk of severely damaging the receiver. However, the objective value of the more robust solution of DET-11 is 11.1% worse than the objective value of DET. Now, the question arises whether this buffer of 11% is suitable. While a high buffer results in poor objective values, a low buffer poses a high risk of severe receiver damage. Furthermore, suitable buffers for each measurement point individually may yield solutions with even better objective values while maintaining a high safety. This is addressed by the more advanced approach of Γ-robust optimization. In Γ-robustness, the degree of robustness is optimized for each measurement point individually as opposed to using the same buffer for all measurement points.

5.3. Performance of Γ-robust solutions

In this part, we concentrate on the objective values and the safety of the Γ-robust solutions from the model presented in Section 4 in comparison to the non-robust solutions. Besides the non-robust problem DET and the buffer problems DET-λ, we now consider the Γ-robust problems for $\Gamma \in \{0, 1, 2, \ldots, 35\}$, denoted by ROB-Γ. For the calculations of the Γ-robust solutions, we first solve ROB-624 by considering it as a non-robust problem with heat fluxes $q_{ha}^{m} = \bar{q}_{ha}^{m} + \hat{q}_{ha}^{m}$ in Constraints (2). Since its solution is also feasible to ROB-35, we use this solution as MILP warm start. Then, we successively use the solution of ROB-Γ as MILP warm start for ROB-$(\Gamma - 1)$ until we eventually reach ROB-1.

Since the robust problems ROB-Γ still have an average gap of 5.86% after 3 hours of running time, this approach is not very practical. Therefore, we additionally use a simple heuristic to get solutions for ROB-Γ in shorter running times. This heuristic first solves the LP relaxation of ROB-Γ where the integrality of all binary variables $x_{ha} \in \{0, 1\}$ is relaxed, i.e., we now have $x_{ha} \in [0, 1]$. Then, all variables that satisfy $x_{ha} < 0.1$ are fixed to zero in the original problem ROB-Γ. Now, the robust problem ROB-Γ is easier to solve since it has far fewer binary variables. We denote the solutions to this simplified robust problem by ROB-H-Γ. To stay within running times of practical relevance, we stop calculations after a maximum time limit of 60 seconds and do not use any MILP warm starts for this heuristic.

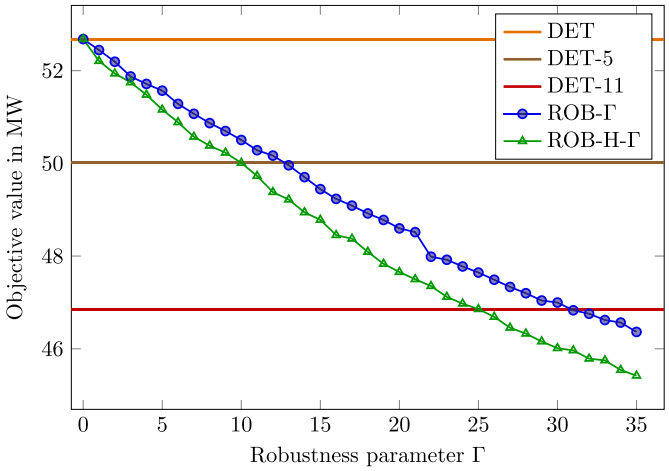

Fig. 3. Objective values of non-robust and robust solutions. The objective values decrease as the buffers in the buffer problems and the Γ values in the Γ-robust problems increase.

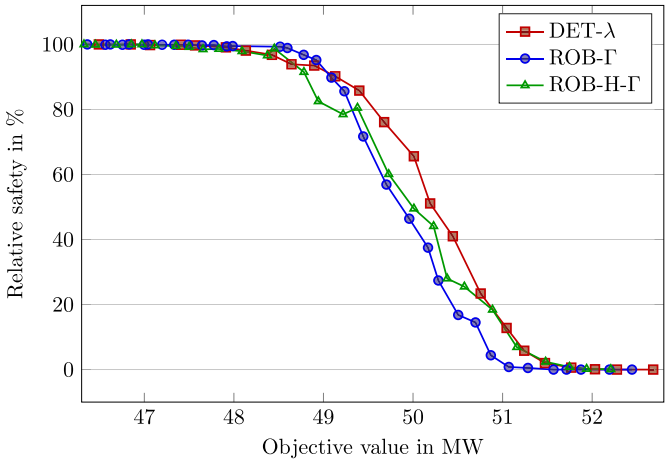

Fig. 5. Pareto front of objective values and relative safety. The buffer solutions DET-λ are stronger for a safety between 0% and 90% while the Γ-robust solutions become competitive for a safety above 90%.

Fig. 3 shows the objective values of the Γ-robust solutions as well as the non-robust and two buffer solutions. As expected, the original non-robust problem DET achieves the best objective value. Adding buffers to the non-robust problem yields worse objective values. DET-5 and DET-11 already lose about 5.1% and 11.1%, respectively, compared to DET. The results of the Γ-robust problems for $\Gamma \in \{0, 1, 2, \ldots, 35\}$ show a similar behavior. Increasing Γ and thus a higher robustness yields lower objective values. While ROB-0 is equivalent to DET, the objective value of ROB-1 is already slightly worse. For low Γ values, the loss compared to DET is relatively small. ROB-10 loses only 4% and even ROB-20 results only in an 8% loss. A loss of 12% is reached at $\Gamma = 35$. The Γ-robust solutions calculated by the heuristic are similar. However, their objective values for the same robust problems are slightly worse. While ROB-H-10 and ROB-H-20 lose 5% and 10%, respectively, a loss of 14% is reached for ROB-H-35.

In Fig. 4, the safety of the Γ-robust solutions in comparison to the non-robust and two buffer solutions is depicted. For each solution, we determined its relative safety by simulating 1000 scenarios. As mentioned in Section 5.2, the solution to DET does not provide any safety while the first secure buffer solution is DET-11 with a safety of 100%. The Γ-robust solutions show that increasing safety is basically achieved by increasing Γ. While ROB-Γ for $\Gamma \in \{0, 1, \ldots, 5\}$ are violated in all scenarios, ROB-6 is the first solution that has a safe scenario. The safety increases rapidly where ROB-18 already achieves a safety of 95%. The first secure solution with 100% safety is reached at ROB-29. Again, the heuristic Γ-robust solutions show a similar behavior. Here, their safety for the same robust problems is slightly higher as they have slightly worse objective values and thus exploit the limits at the measurement points to a less extent. While ROB-H-15 has a safety of 91%, the first solution with 100% safety is already reached at ROB-H-24.

The objective values and relative safety of the solutions are connected in Fig. 5. A Pareto front of these two values is shown for all Γ-robust and buffer solutions. It seems that the buffer solutions are dominating the Γ-robust solutions. Considering the solutions for a safety between 0% and 90%, the buffer solutions have better objective values than the Γ-robust ones while providing a higher degree of safety. However, these lower safety values are not important in practice because we are only interested in solutions with a very high safety close to 100%. Therefore, we show in Fig. 6 the same Pareto front zoomed to the significant relative safety values. Here, we see that the Γ-robust solutions are very strong when we consider a relative safety close to 100%. The best objective values along with a safety between 99% and 100% are all achieved by ROB-Γ. They are clearly dominating the buffer solutions where

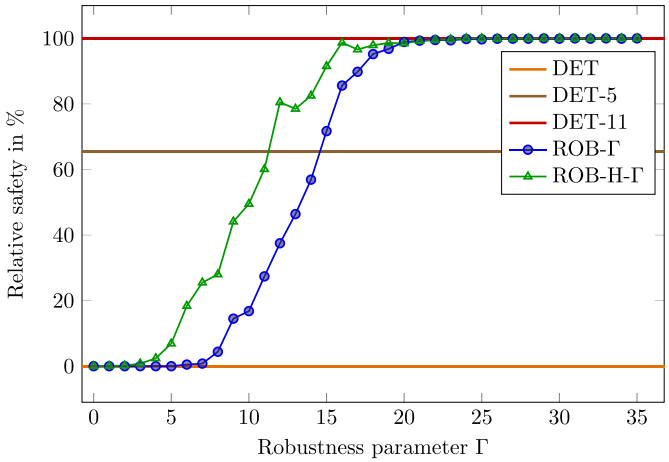

Fig. 4. Relative safety in 1000 simulated scenarios. The safety values increase as the buffers in the buffer problems and the Γ values in the Γ-robust problems increase.

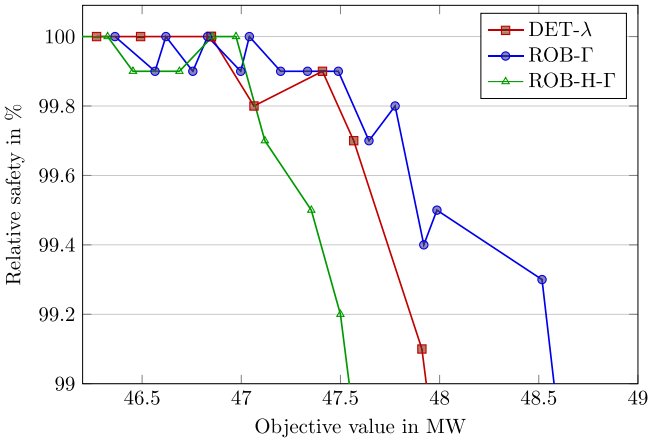

Fig. 6. Pareto front zoomed to significant safety values. The Γ-robust solutions ROB-Γ are dominating the buffer solutions DET-λ within this safety range while the heuristic Γ-robust solutions ROB-H-Γ only beat the buffer solutions for a safety of 100%.

ROB-29 yields the best objective value for a safety of 100%. The Γ-robust solutions calculated by the heuristic show weaker objective values within this safety range. However, they still beat the buffer solutions for a safety of 100% where ROB-H-24 achieves a solution only slightly worse than the best one calculated by ROB-Γ.

Finally, we show the different characteristics of the Γ-robust solutions and the buffer solutions by investigating the slacks of the AFD Constraints (2). Here, the absolute slack S^m at measurement point m is defined as the amount of heat flux that we have to add at m to reach the upper bound in Constraint (2), i.e.,

$$S^m = q^m_{\text{AFD}} - \sum_{h \in H} \sum_{a \in A} q^m_{ha}\, x_{ha} \geq 0.$$

The relative slack s^m at m is given by $s^m = S^m / q^m_{\text{AFD}}$. Fig. 7 shows the relative slacks s^m at each m for four selected solutions. The slacks of the solution calculated by DET are shown in Fig. 7 (a). All relative slacks of this solution are very small with values of less than 1%. This shows that even small deviations caused by tracking errors could exceed the allowable heat fluxes and cause permanent damage to the receiver. The slacks of DET-11, depicted in Fig. 7 (b), all lie between 11% and 11.6%. It is noticeable that the slacks of DET as well as of DET-11 are very homogeneous. On the other hand, the slacks of the Γ-robust solutions show different characteristics. They are not homogeneous anymore. Fig. 7 (c) shows the slacks of ROB-29. They lie between 5.8% and 16% while the measurement points with greater slacks are located in the center of the receiver and the measurement points with smaller slacks are located at the edge. A similar pattern but with slacks between 6.3% and 15% is given by the heuristic Γ-robust solution ROB-H-24, depicted in Fig. 7 (d). This specific distribution of slacks in the Γ-robust solutions occurs because more heliostats can deviate towards the center than towards the edges which exposes the central points to a higher risk of violation. Consequently, this distribution of slacks allows the

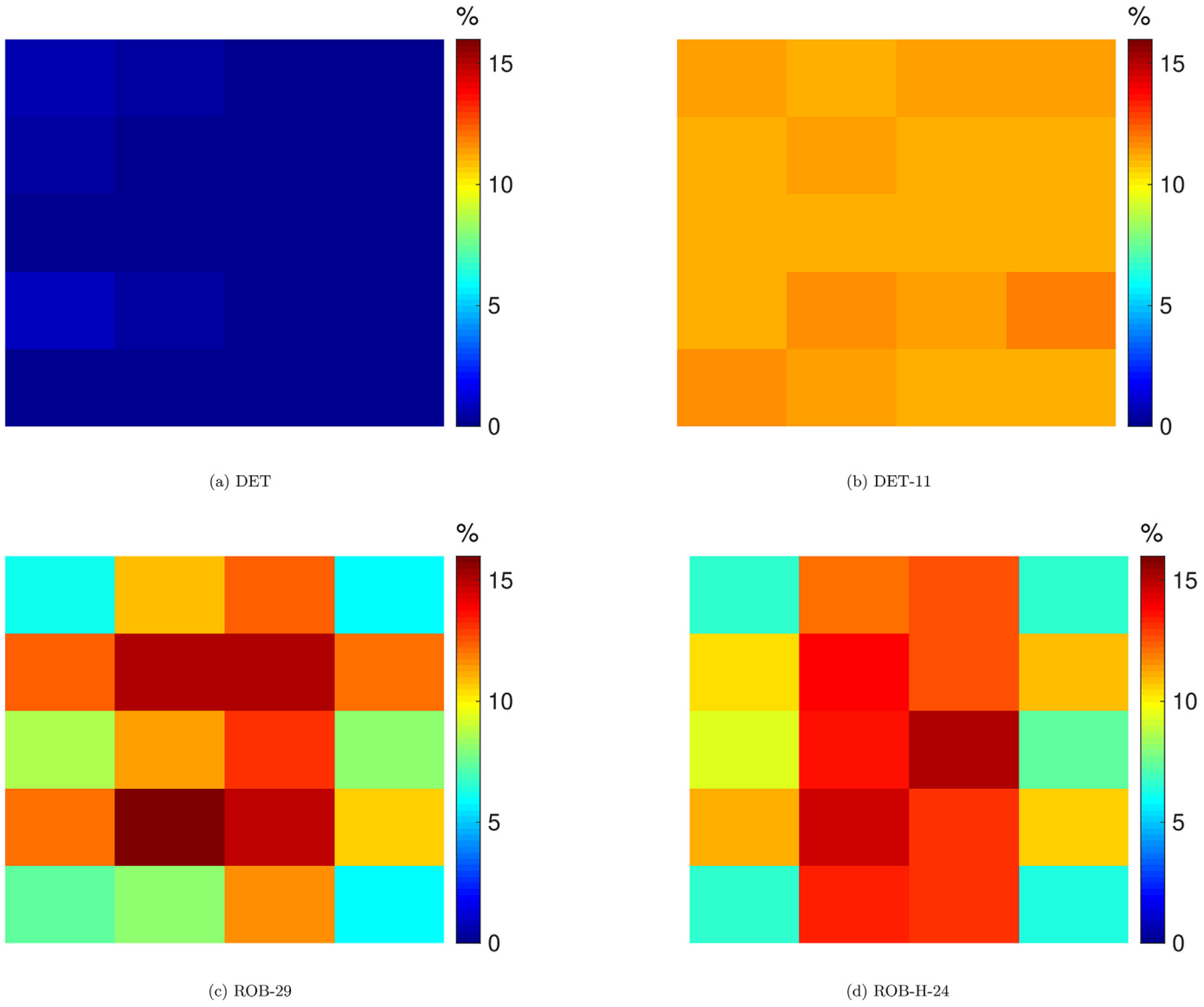

Fig. 7. Relative slacks s^m in AFD Constraints (2). While the slacks in the buffer solutions are very homogeneous, the slacks in the Γ-robust solutions tend to be greater at the central measurement points.

Γ-robust solutions to achieve better objective values than the buffer solutions while providing the same degree of safety.

Detailed results on all computations including their running times, objective values, and safety can be found in the Appendix in Table 2.

5.4. Discussion of the results

This computational study shows the benefits of a robust approach for the optimization of aiming strategies in central receiver systems. We specify the vulnerability of non-robust solutions as well as the effectiveness of Γ-robust solutions.

First, we consider a simple robust approach by adding buffer values to the safety constraints. Then, we compare these buffer solutions to the Γ-robust solutions calculated by our Γ-robust optimization model. To evaluate the safety of the solutions, we perform a simulation of the uncertain tracking errors. It turns out that the Γ-robust solutions are superior to the buffer solutions if we consider the safety values relevant in practice. Finally, we consider the slacks in the Γ-robust solutions which suggest why these solutions are able to provide better objective values than the buffer solutions while having the same degree of safety.

The Γ-robust solutions calculated by ROB-Γ yield very strong results in terms of objective value and safety. Additionally, this approach has even more potential because its best solutions still have an optimality gap of more than 9%. The greatest drawback of the Γ-robust optimization is the running time. Each solution takes a running time of 10800 seconds compared to at most 7 seconds of running time for the buffer solutions. Therefore, we show with the simple heuristic ROB-H-Γ that it is possible to compute competitive Γ-robust solutions within a running time of 60 seconds. This first approach can be improved by more sophisticated ones to compute better Γ-robust solutions within running times of practical relevance.

6. Conclusion

This paper presents a robust approach for the optimization of aiming strategies in central receiver systems. The goal of this robust approach is to increase the efficiency and lifespan of such power plants. To this end, we first present an MILP formulation for the optimization of aiming strategies in the non-robust case. Then, we extend this MILP to a Γ-robust optimization formulation which deals with the uncertainty of tracking errors.

We conduct a case study featuring the PS10 solar tower power plant from Seville, Spain. By performing a simulation of uncertain tracking errors, we show that a robust approach for the optimization of aiming strategies results in economical benefits. The Γ-robust solutions yield strong objective values while providing a high degree of safety for the receiver components. Furthermore, we show that the Γ-robust approach is superior to a simple robust optimization approach which uses buffers at the safety constraints. Finally, we investigate the Γ-robust solutions to explain their strength in terms of objective value and safety.

Future research in this area should focus on improving the solutions of the Γ-robust optimization model. More sophisticated solution approaches should be developed to reduce the running times as well as tighten the optimality gaps. Moreover, the Γ-robust approach should be extended to be able to compute robust solutions for large plants with up to 15000 heliostats such as the Stellio solar field Hami in China [21]. Finally, this robust optimization should be incorporated into a dynamic model with regular update steps to be able to cope with dynamic changes like cloud movement.

Author contributions

Sascha Kuhnke: Conceptualization, Methodology, Software, Writing - Review & Editing, Visualization, **Pascal Richter:** Conceptualization, Methodology, Writing - Review & Editing, Supervision, Funding acquisition, **Fynn Kepp:** Software, Validation, Writing - Review & Editing, Visualization, **Jeff Cumpston:** Conceptualization, Writing - Original Draft, Funding acquisition, **Arie M.C.A. Koster:** Methodology, Writing - Review & Editing, Supervision. **Christina Büsing:** Conceptualization, Methodology, Writing - Review & Editing, Supervision, Funding acquisition.

Declaration of competing interest

The authors declare that they have no known competing financial interests or personal relationships that could have appeared to influence the work reported in this paper.

Acknowledgement

Funded by the Excellence Initiative of the German federal and state governments.

Appendix

Table 2 shows detailed information on all performed calculations. The running times in seconds, the objective values in MW and the relative safety of all buffer solutions DET-λ and Γ-robust solutions are stated.

Table 2
Detailed computational results.

DET-λ				ROB-Γ				ROB-H-Γ			
λ	Time (s)	Obj. (MW)	Safety	Γ	Time (s)	Obj. (MW)	Safety	Γ	Time (s)	Obj. (MW)	Safety
0	6	52.68	0.000	1	10800	52.44	0.000	1	11	52.21	0.001
0.5	5	52.28	0.000	2	10800	52.19	0.000	2	60	51.94	0.002
1	5	52.03	0.001	3	10800	51.88	0.000	3	58	51.75	0.008
1.5	3	51.77	0.006	4	10800	51.71	0.000	4	60	51.48	0.024
2	5	51.47	0.020	5	10800	51.57	0.000	5	60	51.16	0.069
2.5	5	51.24	0.058	6	10800	51.28	0.005	6	60	50.89	0.184
3	6	51.04	0.128	7	10800	51.07	0.008	7	60	50.57	0.255
3.5	4	50.76	0.234	8	10802	50.87	0.044	8	60	50.38	0.280
4	3	50.44	0.410	9	10801	50.70	0.145	9	60	50.23	0.441
4.5	6	50.19	0.511	10	10800	50.50	0.168	10	60	50.01	0.495
5	6	50.01	0.656	11	10802	50.28	0.274	11	60	49.73	0.601
5.5	5	49.68	0.761	12	10801	50.17	0.375	12	60	49.38	0.805
6	5	49.40	0.858	13	10800	49.96	0.464	13	60	49.22	0.785
6.5	5	49.13	0.902	14	10800	49.70	0.569	14	60	48.94	0.825

Table 2 (*continued*)

DET-λ				ROB-Γ				ROB-H-Γ			
λ	Time (s)	Obj. (MW)	Safety	Γ	Time (s)	Obj. (MW)	Safety	Γ	Time (s)	Obj. (MW)	Safety
7	4	48.90	0.935	15	10800	49.44	0.717	15	60	48.78	0.915
7.5	4	48.64	0.939	16	10800	49.23	0.856	16	60	48.45	0.987
8	5	48.42	0.968	17	10800	49.09	0.898	17	60	48.37	0.966
8.5	3	48.13	0.981	18	10800	48.92	0.952	18	60	48.09	0.979
9	5	47.91	0.991	19	10800	48.78	0.968	19	60	47.83	0.986
9.5	3	47.57	0.997	20	10800	48.60	0.989	20	60	47.66	0.985
10	6	47.41	0.999	21	10800	48.52	0.993	21	60	47.50	0.992
10.5	4	47.06	0.998	22	10800	47.99	0.995	22	60	47.35	0.995
11	5	46.85	1.000	23	10800	47.92	0.994	23	60	47.12	0.997
11.5	5	46.49	1.000	24	10800	47.78	0.998	24	60	46.97	1.000
12	4	46.27	1.000	25	10800	47.64	0.997	25	60	46.85	1.000
12.5	5	46.00	1.000	26	10800	47.49	0.999	26	60	46.69	0.999
13	3	45.75	1.000	27	10800	47.33	0.999	27	60	46.45	0.999
13.5	4	45.44	1.000	28	10800	47.20	0.999	28	60	46.33	1.000
14	3	45.19	1.000	29	10800	47.04	1.000	29	60	46.16	1.000
14.5	5	44.94	1.000	30	10800	47.00	0.999	30	60	46.01	1.000
15	3	44.64	1.000	31	10800	46.83	1.000	31	60	45.96	1.000
15.5	7	44.50	1.000	32	10800	46.76	0.999	32	60	45.79	1.000
16	4	44.16	1.000	33	10800	46.62	1.000	33	60	45.75	1.000
16.5	3	43.91	1.000	34	10800	46.57	0.999	34	60	45.54	1.000
17	4	43.59	1.000	35	10800	46.36	1.000	35	60	45.42	1.000

References

[1] P. Richter, Simulation and Optimization of Solar Thermal Power Plants, Ph.D. thesis, RWTH Aachen University, 2017.

[2] T. Dellin, M. Fish, C. Yang, User's Manual for DELSOL 2: a Computer Code for Calculating the Optical Performance and Optimal System Design for Solar-Thermal Central-Receiver Plants, Tech. rep., Sandia National Labs, Sandia National Labs., Albuquerque, NM (USA), 1981. Livermore, CA (USA).

[3] F. García-Martín, M. Berenguel, A. Valverde, E. Camacho, Heuristic knowledge-based heliostat field control for the optimization of the temperature distribution in a volumetric receiver, Sol. Energy 66 (5) (1999) 355–369.

[4] B.D. Kelly, Advanced Thermal Storage for Central Receivers with Supercritical Coolants, Tech. Rep, Abengoa Solar Inc., lakewood, CO, 2010. Report No. DOE/GO18149.

[5] M. Astolfi, M. Binotti, S. Mazzola, L. Zanellato, G. Manzolini, Heliostat aiming point optimization for external tower receiver, Sol. Energy 157 (2017) 1114–1129.

[6] F.J. Collado, J. Guallar, A two-parameter aiming strategy to reduce and flatten the flux map in solar power tower plants, Sol. Energy 188 (2019) 185–189.

[7] B. Belhomme, R. Pitz-Paal, P. Schwarzbözl, Optimization of heliostat aim point selection for central receiver systems based on the ant colony optimization metaheuristic, J. Sol. Energy Eng. 136 (1) (2014), 011005.

[8] S.M. Besarati, D.Y. Goswami, E.K. Stefanakos, Optimal heliostat aiming strategy for uniform distribution of heat flux on the receiver of a solar power tower plant, Energy Convers. Manag. 84 (2014) 234–243.

[9] T. Ashley, E. Carrizosa, E. Fernández-Cara, Optimisation of aiming strategies in solar power tower plants, Energy 137 (2017) 285–291.

[10] D. Bertsimas, M. Sim, The price of robustness, Oper. Res. 52 (1) (2004) 35–53.

[11] P. Richter, F. Kepp, C. Büsing, S. Kuhnke, Optimization of robust aiming strategies in solar tower power plants, in: AIP Conference Proceedings, vol 2126, AIP Publishing, 2019, 030045.

[12] J.A. Duffie, W.A. Beckman, Solar Engineering of Thermal Processes, John Wiley & Sons, 2013.

[13] A. Sánchez-González, M.R. Rodríguez-Sánchez, D. Santana, Aiming strategy model based on allowable flux densities for molten salt central receivers, Sol. Energy 157 (2017) 1130–1144.

[14] P. Schwarzbözl, R. Pitz-Paal, M. Schmitz, Visual HFLCAL - a software tool for layout and optimisation of heliostat fields, in: Solar PACES Proceedings, 2009, pp. 1–8.

[15] P. Richter, M. Frank, E. Ábrahám, Multi-objective optimization of solar tower heliostat fields, in: Progress in Industrial Mathematics at ECMI 2014, Springer, 2016, pp. 357–363.

[16] B. Fortz, M. Labbé, F. Louveaux, M. Poss, Stochastic binary problems with simple penalties for capacity constraints violations, Math. Program. 138 (1) (2013) 199–221.

[17] Abengoa, Solar thermal. http://www.abengoa.com/web/en/negocio/energia/termosolar/. (Accessed 22 August 2019).

[18] R. Osuna, R. Olavarria, R. Morillo, M. Sánchez, F. Cantero, V. Fernández-Quero, P. Robles, T. López, A. Esteban, F. Céron, et al., PS10, construction of a 11MW solar thermal tower plant in Seville, Spain, in: Solar-PACES Conference, Seville, Spain, June, 2006, pp. 1–8. A4–S3.

[19] E. Camacho, M. Soria, F. Rubio, D. Martínez, Control of Solar Energy Systems, Advances in Industrial Control, Springer, London, 2012.

[20] IBM, ILOG CPLEX optimization studio release 12.8.0. https://www.ibm.com/analytics/cplex-optimizer/. (Accessed 22 August 2019).

[21] T. Keck, M. Balz, V. Göcke, F. von Reeken, F. Gross, W. Landman, J. Collado, J. Salas, J. Gracia, J. Iriondo, et al., Hami–the first stellio solar field, in: AIP Conference Proceedings, vol 2126, AIP Publishing, 2019, 030029.